RESEARCH ARTICLE | DECEMBER 21 2020

Wavelength frame multiplication for reflectometry at long-pulse neutron sources

Oliver Löhmann ; Luca Silvi ; Peter M. Kadletz ; Neil Vaytet ; Owen Arnold ; Matthew D. Jones ;
Jonas Nilsson; Michael Hart; Tobias Richter; Regine von Klitzing ; Andrew J. Jackson ; Thomas Arnold ;
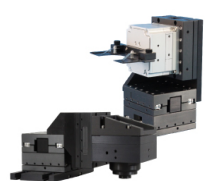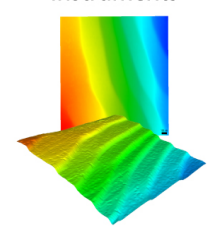Robin Woracek
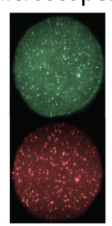
Check for updates

View Online   Export Citation   CrossMark

Wavelength frame multiplication for reflectometry at long-pulse neutron sources

Oliver Löhmann,[1,3,a)] ⓘ Luca Silvi,[2,b)] ⓘ Peter M. Kadletz,[3,c)] ⓘ Neil Vaytet,[3,d)] ⓘ Owen Arnold,[4,5,e)] ⓘ
Matthew D. Jones,[4,5,f)] ⓘ Jonas Nilsson,[3,g)] Michael Hart,[4,h)] Tobias Richter,[3,i)] Regine von Klitzing,[1,j)] ⓘ
Andrew J. Jackson,[3,6,k)] ⓘ Thomas Arnold,[3,4,7,8,l)] ⓘ and Robin Woracek[3,m)] ⓘ

AFFILIATIONS

[1] Technische Universität Darmstadt, Hochschulstraße 8, D-64289 Darmstadt, Germany
[2] Helmholtz-Zentrum Berlin für Materialien und Energie, Hahn-MeitnerPlatz 1, D-14109 Berlin, Germany
[3] European Spallation Source ESS ERIC, P.O. Box 176, SE-22100 Lund, Sweden
[4] STFC, Rutherford Appleton Laboratory, Harwell Campus, Didcot OX11 0QX, United Kingdom
[5] Tessella, Abingdon, OX14 3YS, United Kingdom
[6] Physical Chemistry, Department of Chemistry, Lund University, Box 124, 221 00, Lund
[7] Diamond Light Source, Harwell Science and Innovation Campus, Didcot OX11 0DE, UK
[8] Dept. Chemistry, University of Bath, Claverton Down, Bath, BA2 7AY, United Kingdom

[a)] **Electronic mail:** oliver.loehmann@bam.de. **Current address**: Bundesanstalt für Materialforschung und -prüfung (BAM),
Unter den Eichen 87, 12205 Berlin, Germany.
[b)] luca.silvi@helmholtz-berlin.de
[c)] peter.kadletz@helmholtz-berlin.de
[d)] Neil.Vaytet@ess.eu
[e)] owen.arnold@stfc.ac.uk
[f)] matthew.d.jones@stfc.ac.uk
[g)] Jonas.Nilsson@ess.eu
[h)] mhart@bnl.gov
[i)] tobias.richter@ess.eu
[j)] klitzing@smi.tu-darmstadt.de
[k)] andrew.jackson@ess.eu
[l)] tom.arnold@ess.eu
[m)] Author to whom correspondence should be addressed: robin.woracek@ess.eu

ABSTRACT

The European Spallation Source (ESS), which is under construction in Lund (Sweden), will be the next leading neutron facility with an unprecedented brilliance and novel long-pulse time structure. A long-pulse source not only provides a high time-average flux but also opens the possibility to tune the resolution by using pulse shaping choppers. Thus, an instrument can readily be operated in either a high flux or a high resolution mode. Several of the shorter instruments at the ESS will employ Wavelength Frame Multiplication (WFM) in order to enable a sufficient resolution while offering a continuous and broad wavelength range. A test beamline was operated until the end of 2019 at the research reactor in Berlin to test components and methods, including WFM, in order to prepare the new facility for the operation of neutron instruments and successful first science. We herein demonstrate the implementation of WFM for reflectometry. By selecting a short pulse mode under the same geometrical configuration, we compare and discuss the results for two reference samples. The reported experiments not only serve to prove the reliability of the WFM approach but also, for the first time, demonstrate the full instrument control, data acquisition and data reduction chain that will be implemented at the ESS.

I. INTRODUCTION

Neutrons and x-rays play an important role in the current research for investigating the structure and dynamics of materials and can probe these over several orders of magnitude in length and time. While the scattering interaction of x-rays with matter depends on the atomic number, neutrons interact with the nucleus rather than the electron cloud and hence provide complementary and often unique scattering contrast. In particular, the neutron scattering cross section is isotope specific, and hence hydrogen and deuterium differ strongly allowing for an efficient contrast variation in many scientific applications. Additionally, neutrons have a nuclear spin and a magnetic moment, which enable unique studies of magnetic structures and phenomena, but also some sophisticated scattering techniques such as spin-echo spectroscopy.

Neutron reflectometry is a powerful method to investigate the surface and interface structures, including conclusions about material compositions, on length scales ranging from sub-nanometers up to several hundreds of nanometers. The reflectivity depends on the scattering length density (SLD) profile perpendicular to the sample's surface. Thus, it probes the structure and composition along the surface normal while averaging in the surface plane. Nowadays, neutron reflectometers typically belong to the instrument suites at different facilities spread all over the world[1] and make an important contribution in various research fields, e.g., concerning polymer coatings, energy storage, or magnetism.[2–4] These instruments require a neutron source, in the form of a research reactor or a spallation source. The latter typically offers the advantage of naturally providing a pulsed neutron beam to employ the time of flight (ToF) technique.

The European Spallation Source (ESS), which is under construction in Lund (Sweden), will offer the brightest beam in comparison with today's working neutron sources by providing long neutron pulses of 2.86 ms length at a repetition rate of 14 Hz.[5,6] While the long neutron pulse at the ESS yields a high time average flux, one of the main challenges for reflectometry is the need to obtain sufficient wavelength resolution for the study of thick film structures (around 30-50 nm). It was proposed that Wavelength Frame Multiplication (WFM)[7–9] could be used to deliver this sufficient wavelength resolution and bandwidth, and the design of the reflectometer FREIA at the ESS is based upon this approach.[6,10] The principle operation of WFM is based on running a pulse shaping chopper at an integer multiple of the source frequency, extracting a sequence of pulses each covering a wavelength band, which, when combined, overlaps to leave no gaps in the wavelength coverage. This results in a full bandwidth equivalent to running with no pulse shaping chopper or with one placed very close to the source. In other words, WFM enables a gain in resolution without sacrificing bandwidth at a long-pulse source and moreover offers a high degree of flexibility concerning the resolution.[7–9,11,12] This is especially beneficial for imaging, diffraction, reflectometry, and SANS. Hence, beyond the reflectometry instrument FREIA, other short instruments will utilize WFM from the first day of their operation, such as the imaging beamline ODIN,[13,14] the powder diffractometer DREAM,[15] and the vibrational spectrometer VESPA.[16] While the natural resolution is sufficient for the majority of use cases for the SANS instrument LoKI, it is foreseen that WFM may be a useful upgrade option to improve resolution for certain use cases.[17] In all these cases, showing that WFM data can be reliably collected, converted to effective ToF, and processed using ESS data systems is a vital validation of the method, which will be experimentally demonstrated herein for reflectometry.

Given this novel time structure and because the ESS is a new facility being built on a greenfield site, the ESS operated a test beamline (V20) at the 10 MW research reactor BER II at Helmholtz-Zentrum Berlin (HZB) from 2015 until its closure in December 2019 in order to mitigate against the risks associated with such an undertaking and to allow for the testing of key technologies required to deliver the instrument suite.[18,19] This includes the development of a data collection and processing pipeline, which is able to handle the expected high flux, as well as the systems for instrument control, which are of crucial importance to fulfill the needs of the neutron user community, for example, to handle sampler changers, cryostats, magnets, or fluids.

V20 employed a sophisticated chopper system consisting of two double disk choppers, one for generating a pulsed beam and one for wavelength band selection, as well as four single disk choppers for WFM. The first double disk chopper system was very flexible in providing different pulse lengths but was particularly optimized to mimic the characteristic future pulse shape of the ESS with a long plateau region and a full width at half maximum of 2.86 ms. The flexible experimental endstation allowed for testing a huge array of components and methods, including but not limited to detectors,[20–23] beam monitors,[24] focusing optics,[25] choppers,[26,27] polarization analysis,[28,29] spin-echo modulation,[30] and dark field imaging techniques[30] as well as exploiting the long pulse for scientific investigations.[31,32] In particular, the focus was on experiments that employed WFM and served the purpose of gaining experience with the method in practice, to validate its principles and to develop the data reduction workflow for it.

On V20, sixfold WFM was realized by two disk choppers configured in an optical blind mode (i.e., the first chopper closes when the second chopper opens)[33] that enables constant wavelength resolution throughout the bandwidth. The resolution in such a mode depends on the distance between the two choppers, and thus, to allow for the tuning of the resolution, the inter-chopper distance was adjustable at V20.[18] Here, the long source pulse was divided into six shorter sub-pulses with constant wavelength resolution, which overlap in wavelength but are clearly separated in their arrival time on the detector, as shown in Fig. 1. This yields an increased resolution since each sub-pulse contains a short neutron band with its own start time (t_0^j), with an origin halfway between the two WFM choppers. The combined bandwidth of all sub-pulses is close to the full bandwidth according to the source period.
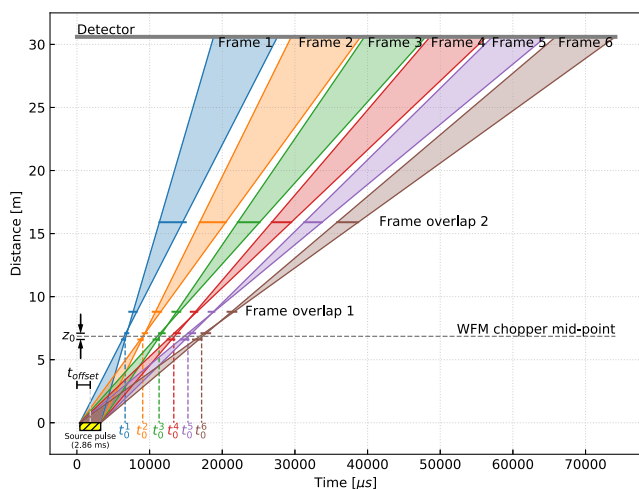
FIG. 1. Time–distance diagram representing the chopper cascade and the position of the detector. The 2.86 ms source pulse (created by the source choppers) is represented by the yellow hatched box in the lower-left corner. The horizontal segments at successive distances from the source choppers represent the openings for the WFM and frame overlap choppers. Note that a horizontal line here corresponds to a chopper being open, instead of being closed, as is commonly found in the literature. The colored areas are bounded by the fastest and slowest neutrons that can make it through each frame. The distance between the two WFM choppers is labeled z_0, while each frame j has its own t_0^j marked by the colored vertical dashed lines.

As WFM is a fundamental principle of several instruments at the ESS, it is important that the method is properly validated. Four key questions about the method can be formulated as follows: (i) Does WFM reach the envisaged resolutions? (ii) Is WFM efficient in reality, or what losses have to be taken into account? (iii) Will the merging ("stitching") of the individual frames create artifacts and/or pose limitations? (iv) Can the data acquisition and data reduction be realized effectively in practice?

Answering these questions has been an ongoing process in recent years. Initially, some proof-of-principle experiments were performed using improvised setups at a continuous reactor source that were able to demonstrate the feasibility of WFM in principle.[34,35] More detailed experimental validations were undertaken at V20 under different experimental configurations. The "V20 commissioning paper"[19] addresses questions (i) and (iii) by demonstrating that neutron transmission spectra of a polycrystalline steel alloy, exhibiting pronounced Bragg edges, can be collected with improved resolution and in a reliable fashion without noticeable artifacts using WFM. The same publication partly addresses question (ii) by comparing the incident neutron beam spectra without the use of WFM to ones obtained with WFM under different resolution settings. More detailed experimental validations have since been performed on V20, in particular for imaging and powder diffraction, and while the analysis is still ongoing at the time of writing this manuscript, separate publications are under preparation that will address questions (i)–(iii) using imaging and powder diffraction test experiments. This manuscript is hence meant to focus on questions (iii) and (iv) for the case of reflectometry. We will show that the WFM concept can be applied in practice to yield quantitative results that compare well

with data collected using the V20 short pulse mode and as well as using the dedicated monochromatic reflectometer, V6, at HZB. Thereby, we also partly address question (i) since the resolution when using the long-pulse mode without WFM would simply not be sufficient to yield the herein reported results. The functionality of software and hardware on V20 was constantly adapted to reflect the development progress of the responsible divisions within the ESS. As this integration has been a step-by-step process, it is worth highlighting that the herein described demonstration experiment utilized, for the first time, the full data pipeline that will be implemented at the ESS, including a centralized timing system, instrument and motion control, electronic logbooks, data acquisition, signal processing, data storage, and data reduction. While these systems had all been tested individually, this integrated testing to perform measurements allowed us to focus on question (iv) and is a significant step toward enabling an operational instrument suite at the ESS. Beyond the above outlined key questions concerning WFM, another contribution of the work presented herein is the development of the general workflow for reflectometry to be implemented at the ESS, namely, the instruments FREIA and ESTIA.

II. EXPERIMENTAL REALIZATION

A. Reference samples

The reference samples were a monochromator sample that was previously measured on an optimized reflectometer and a bare silicon block that has a well-known theoretical reflectivity. Together, these samples allow us to make a direct comparison to our experimental data and thereby highlight any possible inconsistencies. The silicon block [(100), one side polished, $80 \times 50 \times 10$ mm^3] was purchased from Siliciumbearbeitung Andrea Holm GmbH (Tann, Germany) and was cleaned with isopropyl alcohol before the measurement. The second sample was a multilayer that typically serves as a neutron monochromator and hence is referred to in the following as a monochromator sample. It consists of ten bilayers of 5 nm silicon and 10 nm $Fe_{90}Co_{10}$ and was coated with a 5 nm protection layer of silicon. The multilayer was manufactured at Helmholtz-Zentrum Berlin and was deposited on glass with a triode sputter system at a rate of 0.07 nm/s and a pressure of 1.5×10^{-3} bar. Here, silicon grows amorphously, while FeCo grows polycrystalline. The monochromator sample has a nominal area of 150×80 mm^2.

The silicon block should show a well-defined critical edge and a featureless decay with the increasing scattering vector and was chosen since this smooth curve shape will highlight any potential artifacts from the merging ("stitching") of the individual frames in the WFM mode. The interaction of the monochromator sample with neutrons leads to a more complex reflectivity. The monochromator sample itself is a neutron polarizer resulting in a double critical edge for non-polarized neutrons. Furthermore, several Kiessig fringes are present, which are correlated with the overall thickness of the multilayer, while the distance of the Bragg peaks represents the bilayer thickness. The original characterization was done with polarized neutrons at V14 (HZB) as depicted in Appendix A (Fig. 10). Reference measurements with unpolarized neutrons were collected at the V6 reflectometer at HZB as shown in Appendix A (Fig. 11) and are used for direct comparison to data that was collected as part of this work.
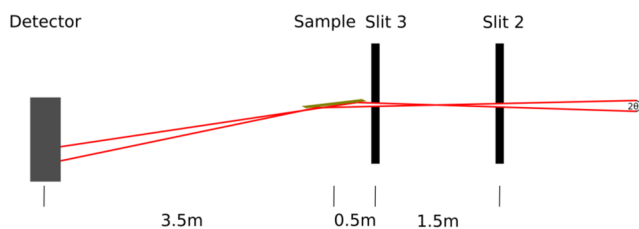
B. Instrumental setup

The ESS test beamline V20 at Helmholtz-Zentrum Berlin was able to mimic the future ESS neutron pulse with a length of 2.86 ms and a repetition rate of 14 Hz. A detailed instrument design and characterization of V20, including verification of the WFM performance, has been described previously.[18,19] Therefore, only an abbreviated description follows, with a focus on the characteristic components. The double disk source pulse choppers (SPCs) were designed to mimic the long ESS pulse including the characteristic plateau but could also be used to provide a shorter or even longer pulse and were located at a distance of 21.7 m downstream from the cold neutron source. The double disk wavelength band chopper was installed at a distance of 31.7 m from the cold source, allowing bandwidths between ~1 Å and 10 Å at the possible detector positions. The center of the optically blind WFM pulse shaping choppers was located at 28.55 m from the cold source, i.e., 6.85 m downstream from the pulsed source. An optical bench with a length of more than 6 m started at 47 m from the cold source and allowed a tailored setup for the respective experiments.

The minimum requirement for a reflectometry experiment consists of two slits for beam collimation and a set of (motorized) stages to align the sample and the detector. A top view of the setup, as implemented on V20, is shown in Fig. 2. The first collimation slit (referred to as slit 2) was placed at the beginning of the optical bench at a distance of 25.1 m from the SPC.

The orientation of the sample surface was chosen to be vertical to maximize the flux when placing collimation slits at the end of the neutron guide. The beam at V20 was more pre-collimated horizontally with the beam profile itself being very inhomogeneous in the horizontal direction.[19] As a result, the flux can be optimized by performing the experiment in this orientation, something that is particularly important for a reflectometry experiment where collimation results in the removal of a significant proportion of the flux. An additional consequence of this orientation is that gravity effects can be neglected.

The collimation slits had a separation of 1.5 m. The sample was on top of a motorized positioning system, consisting of a linear stage, a two-axis goniometer, and a rotation stage, enabling full sample alignment. A position sensitive delay line detector (Denex, Lüneburg, Germany), with an active area of 280×280 mm^2, a spatial resolution of about 2 mm (FWHM horizontally) $\times$ 3 mm (FWHM vertically), and a sufficient time resolution for time of flight measurements, was placed 3.5 m behind the sample.[36] A pixel size of 0.55 mm

TABLE I. Overview of the instrument parameters for the different operation modes. The respective native ESS pulse would have a resolution of 19.1%–3.9%.

Mode	Flight path (m)	Time of flight (ms)	Wavelength band (Å)	Wavelength resolution (%)
1.2 ms SP	30.6	15.0–74.0	1.8–9.4	8.0–1.6
WFM	23.8	13.0–55.0	2.0–9.0	1.8

was assigned to the collected data during the data streaming and event formation process. An overview of the instrument parameters for the different utilized modes is shown in Table I.

In this experimental setup, the long ESS pulse of 2.86 ms length would result in a natural wavelength resolution of 19.1%–3.9% depending on the wavelength, whereas the WFM mode provided a constant resolution of 1.8% for the WFM chopper separation chosen.

For a direct comparison with a more standard data reduction chain, we also performed measurements under the same geometrical conditions, but utilizing the source pulse choppers to provide a short pulse (SP). For the SP mode, the WFM choppers were parked in the open position and the two disks of the source pulse chopper (SPC) co-rotated with a 2° opening, resulting in a pulse with a burst time of 1.2 ms, corresponding to a wavelength resolution between 1.6% and 8.0%. When employing WFM, the ESS pulse was realized by a counter-rotation of the SPC disks. On V20, it was possible to adjust the distance between the two (optically blind) WFM choppers with a corresponding improvement in flux at the expense of resolution, or vice versa. However, it is worth noting that while this is common for chopper systems in the optical blind mode, in the case of the future reflectometer FREIA at the ESS, the spacing between the optically blind chopper pair is fixed.

For this experiment, the two WFM chopper disks had a separation, z_0, of 432 mm resulting in a wavelength resolution of 1.8%. The two frame overlap choppers (part of the WFM chopper cascade) ensured separation of the wavelength frames up to the detector position. In both operation modes, SP and WFM, the wavelength band choppers were used to restrict the wavelength band within the repetition rate of 14 Hz. As discussed by Woracek et al.,[19] the WFM mode on V20 resulted in a narrower overall wavelength band than that of the SP mode, and in this case, the difference was about 1 Å (Table I). The data are presented as a function of the scattering vector Q_z defined by

$$Q_z = \frac{4 \times \pi \times \sin(\theta)}{\lambda}. \qquad (1)$$

Here, θ is the incident angle of neutrons with respect to the sample surface and λ is the neutron wavelength. The wavelength depends on the neutron energy and thus on the ToF and is calculated by

$$\lambda = \frac{ToF \times h}{m_n \times L_{Path}}. \qquad (2)$$

Here, L_{path} is the flight path of neutrons, m_n is the mass of a neutron, and h is the Planck constant.

FIG. 2. Schematic setup of the experiment in the top view. Beam collimation was achieved by two rectangular slits with a distance of 1.5 m. The detector was placed 4 m behind the latter slit, while the sample was placed 0.5 m behind it.

TABLE II. Measurement parameters for the different samples and measurement modes, namely, short pulse (SP) and Wavelength Frame Multiplication (WFM) modes.

| Sample	Mode	Incident angle (deg)	Width of slits 2 + 3 (mm)	Measurement time (min)	Measurement time direct beam (min)	$\Delta Q_z/Q_z$ (%)
Silicon	WFM	0.29	0.2	450	150	3.08
		0.59	0.5	240	35	3.58
Monochromator sample	SP	0.56	0.2	500	152	8.11–2.14
		0.96	1.5	30	11	9.82–5.95
Monochromator sample	WFM	0.56	0.2	470	150	2.22
		0.96	1.5	120	15	5.98

The main difference between SP and WFM modes is the fact that the former naturally results in a continuous wavelength band, while the latter requires additional merging of the dataset. As described in more detail below, all acquired neutron data have been timestamped and—for the work presented herein—been considered and presented relative to the absolute reference time, t_0, from the (main) source pulse. The corresponding procedures to arrive at ToF when using WFM are described in a separate section (Sec. III A) below. Once the data are available at ToF, the subsequent data reduction steps for the two measurement modes, SP and WFM, are essentially the same.

In this study, we aimed at demonstrating that the process employed to arrive at ToF, and hence wavelength, does not introduce systematic and/or problematic artifacts for reflectometry experiments. Since reflectometry measurements cover a very wide range of reflectivities, it is possible that relatively small errors in the corrections could produce artifacts in the finally reduced data that would compromise data analysis. However, since V20 is not optimized for this technique, the flux available for the experiment was significantly limited. We therefore chose collimation settings (see Table II) to maximize the flux while maintaining adequate angular resolution and avoiding over-illumination. Unfortunately, because of the nature of the V20 instrument, the precision and repeatability of the slits used were not well suited to a reflectometry experiment, so there may be small errors in the slit sizes that could result in an

over-illumination of the sample. For each experiment, two angles were measured in order to check that the data reduction process is able to effectively stitch the datasets from the two angular settings together. This is not necessarily required for data analysis but is commonly done for most reflectometry data analysis packages. Since beamtime was limited, the angles were chosen to cover a dynamic range suitable for the samples, within the bandwidth limitations of the measurement mode. For example, the lower angle had an angular resolution of 2.22% in the WFM mode and a footprint of the beam of about 70 mm for the monochromator sample. For the higher angle, the angular resolution was relaxed in order to maintain sufficient flux to obtain a signal of sufficient statistical quality in the time available. This meant that for the monochromator sample, the angular resolution was only 5.98% for a footprint of 149 mm.

C. Data streaming

The data pipeline at the V20 test beamline also acted as a testbed for different systems under development for the ESS. The role of the system is to aggregate all data required to analyze an experiment and write them to a single file. It must also accommodate the high data rates expected due to the high flux at the ESS. An overview of the system deployed at V20 is shown in Fig. 3 and briefly described below. Further details of the ESS data acquisition architecture are given in previous publications.[27,37,38]
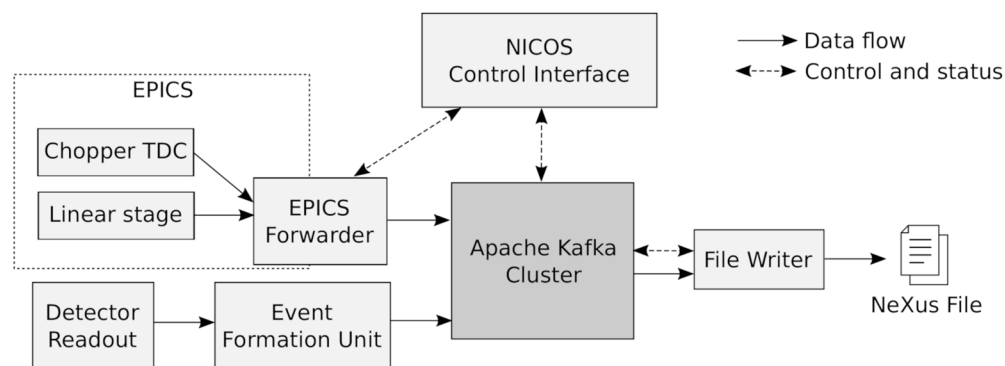
FIG. 3. Overview of the data pipeline at the V20 test beamline.

The Networked Instrument Control System (NICOS)[39] provides a control interface for the user and uses the Experimental Physics and Industrial Control System (EPICS)[40] to communicate with beamline devices. The EPICS supports not only control of devices but also monitoring their state. Data acquisition was carried out this way on V20 for measurements from a range of devices, including top-dead-center (TDC) signals of neutron choppers and positions of linear motion devices. Since the integration of devices with the EPICS is necessary for control, it also provides a convenient approach for the acquisition of low bandwidth data such as sample environment measurements; however, it is not so well suited to lossless communication of high bandwidth data such as neutron detection events. We therefore also employ the Apache Kafka data streaming platform.[41] In a Kafka-based streaming system, all software publishes data to, or consumes data from, named data streams on a server called a "broker." This gives rise to a conceptually simple architecture that avoids creation of a complex web of directly connected software, which can be difficult to configure and maintain. Another advantage is that the broker provides a buffer so that data are not lost if consumers of data cannot keep up with peak data production rates, or even if they fail part way through an experiment run. Although only a single Kafka broker was deployed at V20, Kafka supports adding more brokers to form a cluster. This solves potential problems with communicating through a single piece of hardware and software, including being a bottleneck for data throughput and being a single point of failure for the entire data system. In fact, a single cluster comprising many brokers can robustly support the data throughput of an entire neutron facility of many beamlines.

The "Detector Readout," see Fig. 3, originates with output signals from the delay line detector. These were passed through a discriminator (Five Channel Timing Discriminator, Model 715, Philips Scientific[42]) and in turn fed to four time-to-amplitude converters (TACs, 566 Time-to-Amplitude Converter, ORTEC, Oak Ridge, USA[43]) to convert cathode-to-anode delay for all four anode outputs to a voltage. The output of the TACs was digitized and time-stamped using the ESS detector readout demonstrator.[44] These data were then processed using ESS developed event processing software in the "Event Formation Unit".[45]

The ESS detector readout demonstrator digitizes the full waveform of the pulses produced by the TACs, and thus, the first step in the event processing software is to extract the amplitude of the pulse from the data. The amplitudes from the four TACs are correlated in time in order to find pulses that represent a neutron event. When pulses from all four TACs have been found in a narrow time window (~1 μs), the amplitudes can then be used to calculate the position of the neutron event in the detector. Finally, the position information together with the absolute timestamp of the neutron event is transmitted to the Kafka broker.

While neutron event data are published directly to Kafka, the "EPICS Forwarder" monitors the state of devices and publishes updates to the cluster such that all measured data are aggregated. The NICOS controls the "File Writer" by publishing start and stop events of each experiment run, along with further details including what data should be retrieved from Kafka and information that does not change during an experiment, for example, the size and position of pixels in the detector. After being triggered by a start event, the File Writer consumes data from Kafka and records each experiment

to an HDF5[46] file in the NeXus format.[47] All data required for analysis of an experiment are thus recorded to a single file, which can be read later by reduction and analysis software such as Mantid[48] or Scipp.[49]

III. DATA REDUCTION

The data reduction for the present work was performed with Python scripts using the Mantid framework.[48] In this section, we will outline in detail the method used to calculate ToF from recorded neutron event timestamps when WFM choppers are in use. We will next describe the utilized regions-of-interest and corresponding background corrections, and finally, we will present the resulting resolutions.

A. Converting WFM data to time of flight and wavelength

As described above, all neutron data are recorded in the event mode with absolute timestamps. In order to generate meaningful ToF spectra, each neutron event needs to be related to a correct start time. While data recorded in the SP mode naturally yield continuous ToF spectra with respect to the start time of the source pulse, the data recorded using the WFM mode result in discontinuous spectra, since the individual openings of the WFM pulse shaping choppers act as new source pulses, each one producing a wavelength frame with its own start time.

The first post-processing step that *all* recorded files were put through to calculate the event ToFs from detector timestamps used the original source chopper timings as a start time, regardless of whether WFM choppers were in use or not. Recorded ToFs for WFM runs thus need to be converted to actual ToFs by subtracting each frame's own start time from the recorded ToFs. This procedure allows us to reconstruct a continuous (actual) ToF spectrum from the six WFM frames, even though the frames appear to have "gaps" between them in the raw recorded data and in the time–distance diagram (Fig. 1). Subsequently, the wavelength can be calculated straightforwardly by using the distance between the WFM choppers and the detector as the corresponding flight path.

At the time of writing this manuscript, the recorded to actual ToF conversion for WFM runs is still a work in progress, and two separate methods have been developed at V20. The first, the most established and tested version, involves using peak finding to detect the frame edges on the recorded data. This can be categorized as an "empirical" procedure, by working on the raw data that were recorded. The second method can be categorized as a more "predictive" or "analytical" approach, whereby knowledge of the instrument geometry is used to construct time–distance diagrams (such as the one pictured in Fig. 1), which in turn allow us to determine both the boundaries of the frames and the t_0 shifts that need to be applied to each frame. This is a recent development in the ESS software suite and is still under testing. In this work, we employed the first, well tested procedure to perform data post-processing.

At this point, we like to make an important distinction between "stitching" data from different reflection angles to obtain a greater coverage of the Q_z-range and "stitching" the frames in a WFM dataset into a continuous spectrum. The former is a common usage
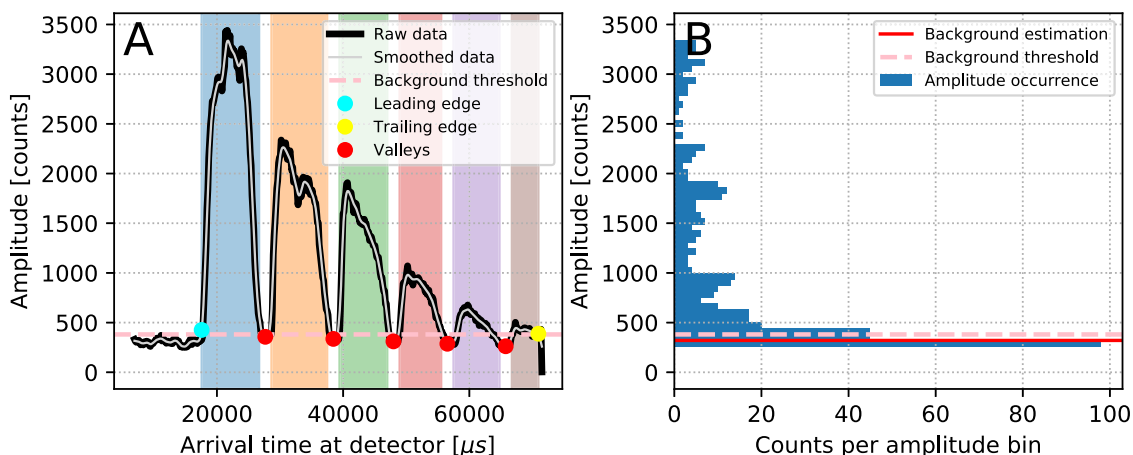
FIG. 4. (a) Raw data from a reflectometry experiment at V20, showing the six WFM frames in different colors, as well as various markers that illustrate the steps in the frame finding algorithm (refer to the main text). (b) Histogramming of counts in amplitude bins to detect the background as the most common count occurrence.

of the word "stitching" in reflectometry, and to avoid any confusion in this work, we will employ the term "WFM to ToF conversion" for the latter one.

The first part of the procedure consisted of detecting the boundaries of each sub-frame in the data. Peak-finding algorithms usually require a good signal-to-noise ratio, and the neutron counts from all pixels were therefore histogrammed into a single spectrum, giving the characteristic segmented spectrum, shown as a black curve in Fig. 4(a). The spectrum was then smoothed using a Gaussian filter with a standard deviation of 2 (gray curve).

Peak finding also requires a good estimate of the level of background noise of the processed signal. We wish to point out here that this background is along the time dimension and is completely independent of the background subtraction performed in Sec. III C. This background is only used in this edge-finding step and is not subtracted from the experimental data. The background noise estimation was carried out by histogramming the neutron counts in number-of-occurrence bins, to find the most common count in the data. This will almost always be the background, which shows a high occurrence of very low counts, as can be seen in Fig. 4(b) (red dashed line). This raw background value was modified in a conservative way by adding to it 2% of the range between the raw background amplitude and the maximum amplitude in the data. This updated background value is represented by the pink dashed line.

The leading (left) edge of the signal was then found by iterating through the spectrum, starting from the left-hand side and finding the first data point that exceeds the updated background value. This edge is marked by a blue dot in Fig. 4(a). The same was repeated for the trailing edge (yellow dot), starting from the right-hand side and iterating toward the left. The next step was to find five valleys (or inverted peaks) between these two edges. A peak-finding algorithm from the SciPy library[50] was called on the inverted data (to find the valleys). The prominence parameter was given a value of $0.04 \cdot (signal_{maximum} - signal_{minimum})$. The five valleys are marked with red dots in the left panel.

We defined exclusions regions that were 1950 μs-wide around each red dot, to set the boundaries of the frames. The value of 1950 was obtained from trial and error, giving an optimal balance between minimizing frame overlap and minimizing event elimination. The leading (blue dot) and trailing (yellow dot) edges then complete the set of frame boundaries.

The second part of the procedure involved determining the time shifts (t_0^j) that needed to be subtracted from each frame to obtain a continuous ToF spectrum. While in principle t_0 for each frame is known from the instrument geometry and chopper properties (angular openings, rotation frequencies, and phases relative to the source chopper), as illustrated in Fig. 1, in practice, the predictions do not line up with the measurements. Some additional time offsets, most probably due to timing delays in electronics and detector readouts that are unaccounted for in the time–distance diagram, were needed to yield good results.

The time shift for the first frame was experimentally determined by separate calibration measurements using standard powder samples in diffraction as well as an iron powder sample in transmission geometry. The time shifts for frames 2–6 were calculated with respect to frame 1, using chopper cut-out angles and rotation frequencies, according to Eq. (3) in the study by Woracek et al.[19] The resultant time shifts used for the current data are listed in Table III.

Figure 5 shows the results from converting a direct and reflected beam to ToF. Some troughs in the signals are visible at the boundaries between frames. It is a concern that these discontinuities (hereafter referred to as WFM to ToF conversion artifacts) could be

TABLE III. Time shifts (t_0) applied on the measured data.

Frame number	1	2	3	4	5	6
Shifts (μs)	−6630	−9054	−11307	−13364	−15313	−17154
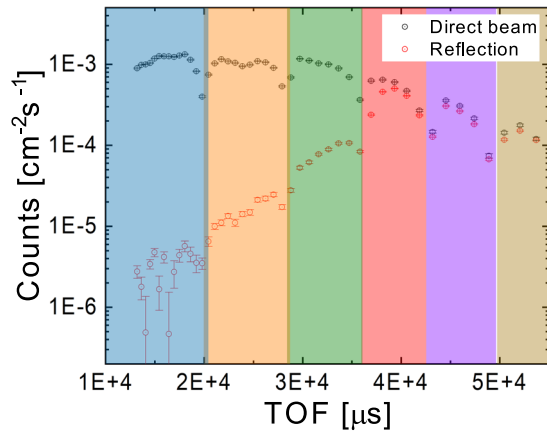
FIG. 5. Data of the direct beam (black squares) and reflection of a bare silicon wafer after WFM to ToF conversion (red dots, angle of incidence: 0.29°). Different background colors highlight the six individual sub-frames.

visible in the reduced data. However, they disappear once the specular intensity is divided (or normalized) by the direct beam intensity (see below). For this procedure to be successful, it is also obvious that also other experimental factors need to work smoothly in order to avoid systematic artifacts in the processed data, e.g., the detector response needs to be linear across the dynamic range.

B. Resolution and ToF bin sizes

The resolution function of the scattering vector $\frac{\Delta Q_z}{Q_z}$ has two main contributions: angular and wavelength resolution.[51] The angular resolution $\frac{\Delta \theta}{\theta}$ is defined by collimation, the sample angle resolution, and potentially the detector resolution, while the wavelength resolution $\frac{\Delta \lambda}{\lambda}$ is defined by the burst time of the pulse, the flight path length, and potentially the detector time resolution. Van Well *et al.*[51] reported a definition for the angular resolution as

$$\frac{\Delta \theta}{\theta} = \sqrt{0.68^2 \left(\frac{d_1^2 + d_2^2}{l^2} \right)} / \theta, \tag{3}$$

where d_1 and d_2 are the width of the collimation slits and l is their separation. For the short pulse mode on V20, the wavelength resolution is wavelength dependent and defined by the burst time τ (note that while τ is independent of λ at V20, this is not necessarily true for a spallation source) and the time of flight (ToF) of the respective neutron and can be written as

$$\frac{\Delta \lambda}{\lambda} = \frac{\tau}{ToF(\lambda)}. \tag{4}$$

When employing the optically blind WFM pulse shaping choppers, τ and ToF have the same linear wavelength dependence within each wavelength frame,[33,51] hence providing a constant wavelength resolution for the combined wavelength band.[14,18] Here, the wavelength resolution is defined by the distance z_0 between the two WFM choppers and the flight path of the neutrons, which can be expressed as

$$\frac{\Delta \lambda}{\lambda} = \frac{z_0}{L_{Path}}. \tag{5}$$

In total, the resolution in Q_z results in

$$\frac{\Delta Q_z}{Q_z} = \sqrt{\left(\frac{\Delta \lambda}{\lambda} \right)^2 + \left(\frac{\Delta \theta}{\theta} \right)^2}. \tag{6}$$

The resolutions of the different settings are summarized in Table II. The spatial resolution of the detector does not affect the experimental resolution because neutrons are summed up over an area larger than the spatial resolution. The bin sizes were calculated out of the instrumental resolution for each measurement according to the resolution as described in Table II. The bin widths were calculated iteratively starting from the beginning of each ToF-range by setting the bin width to the resolution.

C. Regions-of-interest and background correction

Data reduction was based on 2D detector images, as shown in Fig. 6. A mask was applied on the image to focus on the important field of view as highlighted by the black rectangle. In the y direction, the data were confined close to the signal. The choice of the size of
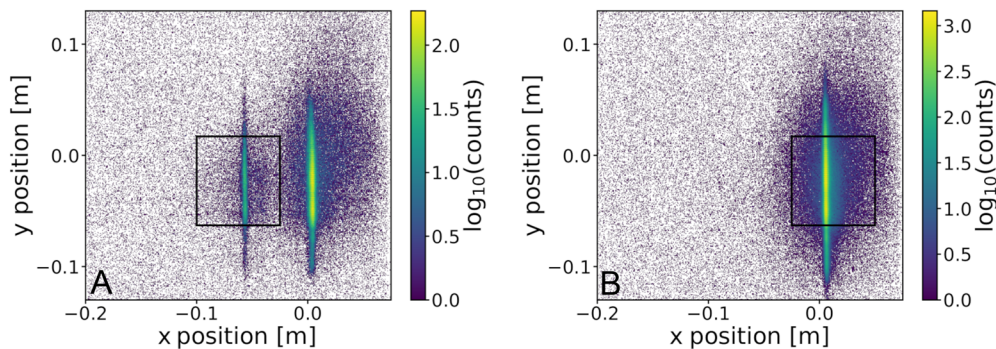
FIG. 6. Two 2D detector example images of a sample measurement (a) and the open beam (b). In these images, x is the horizontal position and hence the direction of scattering from the sample. In both images, the direct (unreflected) beam can be seen, while on the left, the reflected beam is also observed. All ToFs are summed up to determine the boundaries for a region marked by a black rectangle.
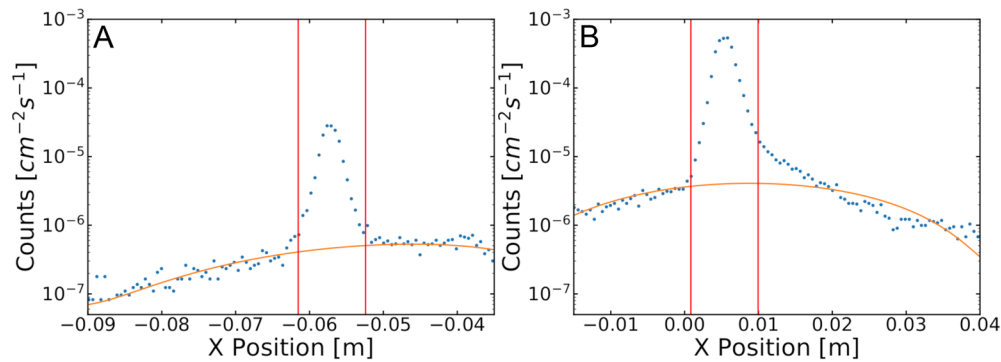
FIG. 7. Two example histograms of a reflection (a) and a direct beam (b). Data are shown by blue dots, the background fit is shown by orange lines, and the range of interest is marked by two vertical red lines.

this box in the y direction must balance the need to capture the full specular reflection against the signal-to-noise ratio. A larger box may capture more of the signal, but it also captures more background. In the x direction, a larger area was selected/retained to allow for subsequent background correction. Afterward, all data were normalized by their area and the integral of a neutron monitor, which was placed directly after slit 2.

After ToF binning, histograms along the x direction were generated by summing up the counts in the y direction. The bin size was defined by the Q_z resolution as described above. The histograms for each bin allow for a background correction, as shown in Fig. 7. A range of interest (ROI) marked by two vertical red lines in Fig. 7 was derived from a Gaussian fit to the signal. The ROI width of the reflection signal was set to three times the standard deviation to collect at least 99.7% of neutrons contributing to the signal. The ROI width of the direct beam was adopted from the corresponding reflection. The background was fitted to the data outside the ROI to a fourth order polynomial. Afterward, the integral of the background inside the ROI was subtracted from the integral of the signal.

After background correction for each individual time bin, the data are divided by the respective direct beam resulting in reflectivity. The ToF is converted to Q_z according to Eqs. (1) and (2). The final data were corrected by a scaling factor in R, but the unscaled data are shown in Appendix B. The scaling factor was determined to be 1.18 by shifting the plateau of the silicon data to unity and was applied to all measurements (both WFM and SP modes). It is not clear what the origin of this scaling is, but it is the same for all measurements. Finally, data of the respective sample measured under different angles were combined to obtain a complete dataset.

IV. RESULTS

A key result of this test experiment was the successful implementation of the data pipeline with data from all measurements written into NEXUS files. This is the first demonstration of the working data pipeline and instrument control system that will be implemented at the future ESS. The data recorded using the SP mode naturally yield continuous ToF spectra with respect to the start time of the source pulse. Timing corrections were implemented to

compensate for time offsets introduced by detector readout times and electronics. The data recorded using the WFM mode result in discontinuous spectra with respect to the start time of the source pulse. As explained above, for the herein presented results, a post-data reduction algorithm was written and applied to obtain continuous ToF for the WFM data. An example is shown in Fig. 5. This will be the basis for the future implementation of WFM systems on ESS instruments, including the reflectometer FREIA.

A. Silicon block

Figure 8 shows the data of the bare silicon block measured with WFM and compares them to the Fresnel reflectivity of a silicon substrate. The data are a combination of measurements under two incident angles and corrected in R to scale the plateau below the critical edge to 1. The data before scaling and stitching of the two angles are shown in Appendix B (Fig. 12). As a first qualitative result, one can conclude that the curve looks like the theoretically expected one. Importantly, discontinuities are not visible and the data decay
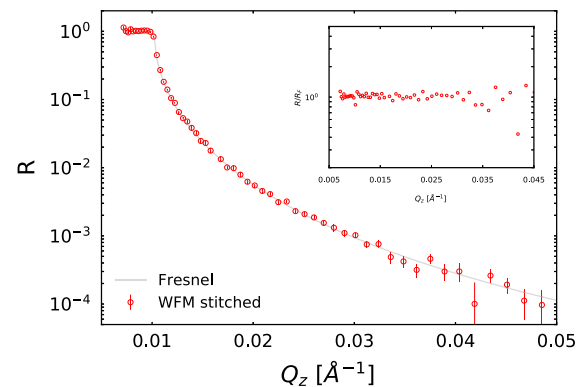
FIG. 8. Combined data (red circles) measured with the ESS pulse in the WFM mode compared to the Fresnel reflectivity of a silicon block (gray line). Inset: data divided by the Fresnel reflectivity. The dataset consists of measurements under two incident angles and is scaled so that the plateau value is unity.
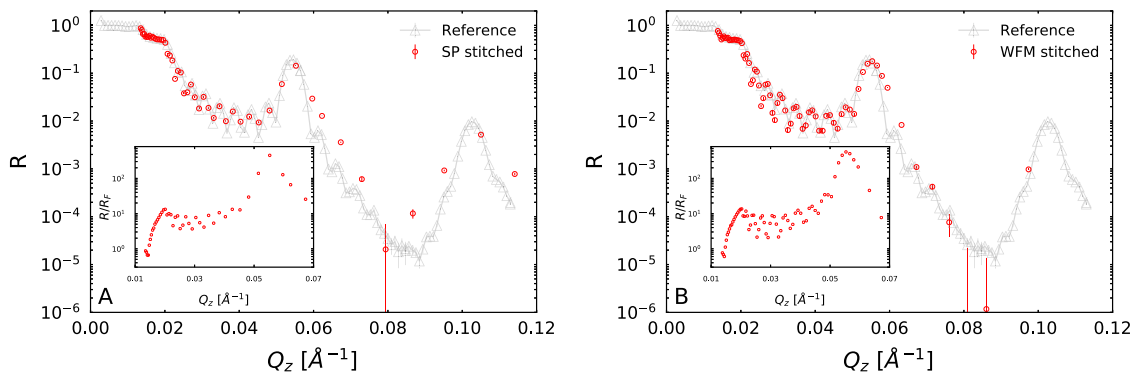
FIG. 9. (a) Reflectivity data of the monochromator sample measured in the short pulse mode. Inset: data divided by the Fresnel reflectivity of the glass substrate. (b) Reflectivity data of the monochromator sample measured in the WFM mode. Inset: data divided by the Fresnel reflectivity of the glass substrate. Both datasets consist of measurements under two incident angles and are scaled using the same factor obtained from scaling the data from the silicon block.

monotonically above the critical edge. This observation proves that the data reduction procedure applied to the originally discontinuous WFM dataset is adequate. Unfortunately, the Q_z-range measured does not allow for a quantitative fitting of the reflectivity. As can be seen in Fig. 8, the curve follows very closely the Fresnel reflectivity of silicon (i.e., R/Rf = 1). Over this Q_z-range, such a dependence could also be seen for a rough silicon oxide layer, and it is hence not possible to uniquely fit the data. However, a rough sample is qualitatively consistent with the sample history, which was neither purchased exclusively for this experiment nor extensively cleaned.

B. Monochromator sample

Figure 9 shows the data of the monochromator sample measured with a short pulse (a) and a ESS pulse in the WFM mode (b). The data before scaling and stitching of the two angles are also shown in Appendix B (Figs. 13 and 14). Data, measured at the monochromatic reflectometer V6 (HZB), are shown in gray for comparison.

All data overlay well up to the first Bragg peak at 0.055 Å^{-1} and show at least six well pronounced Kiessig fringes between 0.02 Å^{-1} and 0.05 Å^{-1}. In fact, the data in the low Q_z-range (up to 0.027 Å^{-1}) show evidence of improved resolution relative to the reference monochromatic measurements made using V6. Deeper minima and even a seventh Kiessig fringe are visible for the current ToF measurements, for both SP and WFM modes. In contrast, the Bragg peaks measured at V20 are broadened relative to those at V6. It is also notable that the Bragg peak measured at V20 using WFM is even broader than that measured using the SP mode. At high Q_z, above the first Bragg peak, the data in both ToF modes are smeared out in comparison with the reference data. All of these features are due to the wavelength dependence of the resolution function for the SP mode and the difference in bandwidth of the two modes. For the SP mode, the wider bandwidth means that the first Bragg peak occurs within the Q_z-range covered by the first measurement angle for the respective dataset. Covering the Bragg peak with the first measurement angle with its higher resolution with respect to

the second measurement angle leads to a better Q_z resolution in the respective range. This is not the case for the WFM mode, where the data of the first measurement angle end right after the maximum of the Bragg peak. Thus, most of the significant reflectivity curve (all fringes and >50% Bragg peak, compare Fig. 14) is covered by the data with high resolution, but the Bragg peak is not fully covered with sufficient data points. Nevertheless, the data of the second angle show a decreasing trend with increasing Q_z between 0.06 Å^{-1} and 0.09 Å^{-1}. In both ToF modes, the angular resolution for the second angle is significantly worse than that for the V6 measurement, which results in a broader Bragg peak in the stitched data and fewer data points. Finally, the overall shorter Q_z-range for the WFM data is a result of the shorter wavelength band compared to the short pulse measurements (see Table I).

V. DISCUSSION

The ESS test beamline was designed as a multipurpose instrument with a focus on providing the future ESS pulse structure including a WFM option, acting as an instrument control testbed and data pipeline. It was not, however, optimized for reflectometry. In particular, this means that several compromises were required to perform this experiment. The large cross section of the neutron guide (60 × 125 mm^2) provided high flux and flexibility, e.g. for imaging experiments, but it was less well suited to reflectometry since the flux obtained through the tight collimation required for reflectometry was relatively low. Furthermore, the ad hoc slits and sample alignment stages used were not well suited to this technique and resulted in some uncertainty in the angular resolution and footprint on the sample surface. After data reduction, a scaling factor was required to bring the total reflection of the silicon data to unity. While we cannot identify the cause of this scaling, we can be sure that it is not due to the WFM data treatment since the same scaling factor is required for both the WFM and SP modes. In fact, it is also notable that the discrepancy between the direct beam and the reflected intensity is visible in Fig. 5 (in the fifth and sixth subframes), demonstrating that this factor is present in the raw data. It must, therefore, be due to the non-ideal experimental setup rather

than the data treatment. Finally, the overall flux after collimation was limited, and as such, we were forced to compromise on resolution for the second angle in order to make measurements within the available beamtime.

Despite these drawbacks, reflectometry was possible using WFM on two different samples. The data were of high enough quality to develop and test different WFM to ToF conversion procedures, one of which was presented herein in detail. As this process entails merging of discontinuous datasets in the form of several wavelength frames into one continuous wavelength band, it is the frame boundaries that are potentially prone to systematic artifacts. In this study, any inconsistency in the data acquisition and reduction procedure would immediately be revealed by minima and/or maxima in the signal after normalization by the direct beam. When looking at the herein obtained final data, it is clear that they compare well with the reference data and, importantly, WFM to ToF conversion artifacts are not visible.

The resolution function has two main contributions, namely, the wavelength resolution $\frac{\Delta\lambda}{\lambda}$ and the angular resolution $\frac{\Delta\theta}{\theta}$. In general, ToF experiments have a better resolution at low Q_z in comparison with monochromatic experiments (0.2 Å^{-1} on V6).[52] This is because ToF instruments are generally able to use much longer wavelengths than those typically provided by monochromatic instruments. Therefore, for any given minimum Q_z, θ is smaller for the monochromatic instrument, and so, $\frac{\Delta\theta}{\theta}$ is relatively larger. Due to the long native ESS pulse and correspondingly poor wavelength resolution, most of the features observed in our data here would not be visible without the use of WFM. As shown in Figs. 8 and 9, the measurements reproduce the Fresnel reflectivity of the silicon substrate (at least over the limited Q_z-range measured) and compare very well to the reference data of the same monochromator sample measured with an optimized, monochromatic instrument. The frame transitions are visible in the data after WFM to ToF conversion (see Fig. 5) but vanish after division of the specular intensity by its incident beam. This proves that the conversion to the ToF procedure performs effectively and without visible artifacts.

VI. CONCLUSION AND OUTLOOK

The ESS will be one of the leading neutron sources with an outstanding high flux and a long-pulse time structure. By using pulse shaping choppers, the long pulse will allow for a high degree of flexibility when it comes to customizing the instrument performance in order to provide the optimal balance between flux and resolution—much more so than is possible at a short pulse neutron source. The instruments of shorter physical length at the ESS can optimally exploit a larger wavelength bandwidth compared to the longer instruments, and when a higher wavelength resolution is required, they employ pulse shaping by Wavelength Frame Multiplication (WFM).[6] While employing WFM allows for the use of a broad and continuous wavelength band at increased resolution, it requires an additional merging of the dataset compared to running without it. In this work, we have experimentally demonstrated that the WFM concept works for reflectometry measurements. Although the ESS test beamline V20 was not optimized for reflectometry, the results are comparable to those obtained on a well-established instrument.

Furthermore, the data presented herein were obtained by using the full data pipeline and instrument control as will be implemented in the future ESS instruments. Establishing and verifying this workflow was—for the first time—successfully achieved for the present experiments. This was only possible due to the close and fruitful collaboration of instrument scientists, software developers, and engineers. Given the multinational collaboration structure of the ESS and being a new facility, maturing the herein demonstrated interplay between divisions and partner institutes is one of the important steps for the ESS to ensure successful commissioning and early science once the facility starts to operate in 2023.

The WFM specific data reduction was implemented herein as a post-process data treatment. The conversion of the individual subframes to ToF works in a robust manner and will be the basis for future fully automatic data treatment. Another future possibility of treating data obtained in the WFM mode foresees that the event-by-event conversion to ToF is performed as part of the event formation unit or the file writer. In such a case, one would write the raw and stitched data files simultaneously, thus cutting out the time needed to re-read the raw data to perform the conversion. Details will be presented and discussed in following publications.

WFM is planned for the ESS reflectometer FREIA, and the instrument will hence directly benefit from this study, as will all instruments that employ WFM since they will make use of the same data processing pipeline. In addition, the whole ESS instrument suite will benefit from the practical experience gained concerning data streaming and instrument control that is now to be implemented during the construction of the individual instruments before they start hot commissioning.

APPENDIX A: REFERENCE DATA

One of the used samples was a well characterized neutron monochromator sample manufactured at Helmholtz-Zentrum Berlin. This monochromator sample is a neutron polarizer and interacts differently with neutrons of different spin states. A full
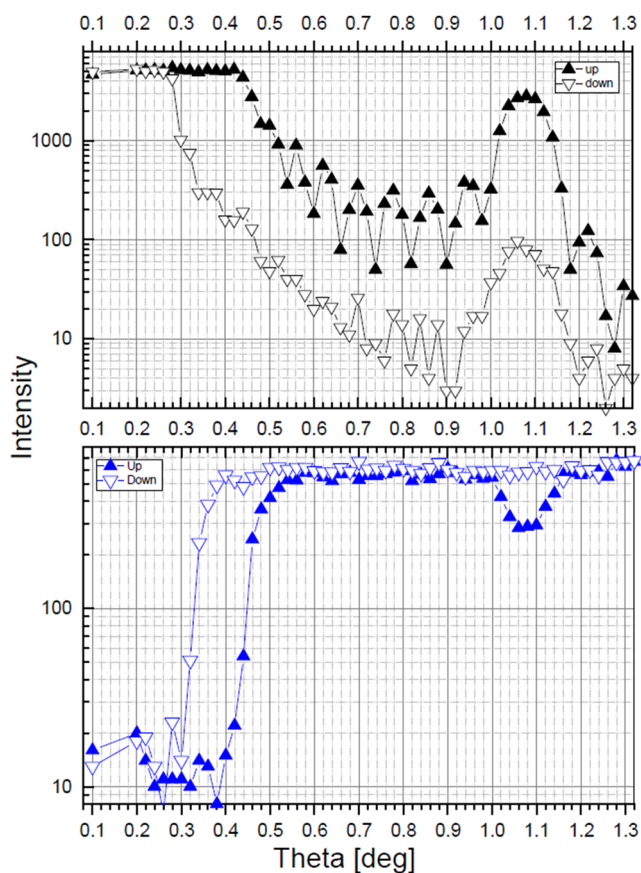
FIG. 10. Data obtained from the V14 instrument at HZB measured with polarized neutrons (λ = 4.7 Å) and with a magnetic field of 300 G. (a) Reflectivity measured with up (closed symbols) and down (open symbols) spin states for different angles. (b) Transmission measurements with same instrument settings.

characterization was done previously on V14 at HZB. The data are shown in Fig. 10. A magnetic field of 300 G was applied, and the monochromator sample was measured with neutrons in spin-up and spin-down states from 0 to 1.3°.
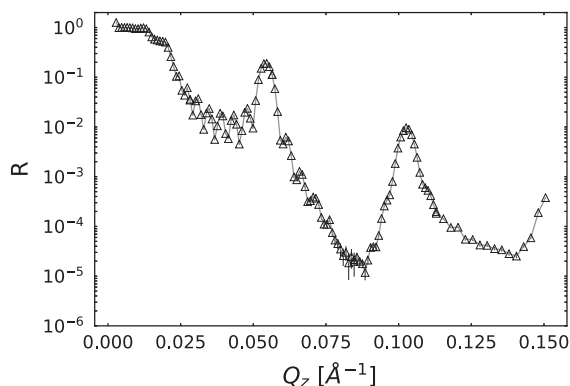
FIG. 11. Data obtained from the V6 instrument at HZB measured with unpolarized neutrons (λ = 4.7 Å).
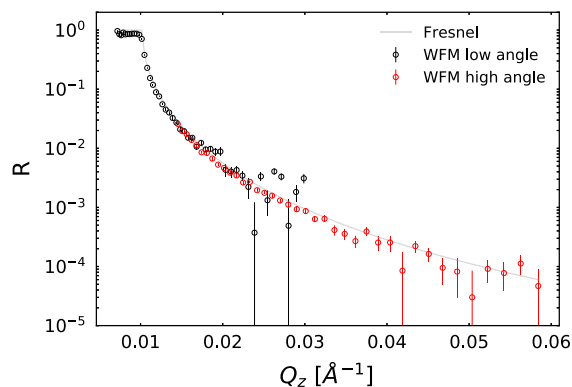
The measurements at V20 were carried out with unpolarized neutrons. Thus, the data were compared with data obtained with a dedicated reflectometer (V6 at HZB) measuring with unpolarized neutrons. The data from V6 are shown in Fig. 11. Due to the unpolarized neutron measurements at V6, the resulting data reflect a sum of the two spin states measured at V14. Thus, two critical edges are visible.

APPENDIX B: REFLECTOMETRY DATA

Reflectometry data obtained by ToF experiments are usually measured using 2–3 different angles depending on the available bandwidth in order to cover the desired Q_z-range. Since most current analysis packages require a continuous curve, the data from each of these angles are generally stitched together over the desired Q_z-range. To do this, the data are overlapped in Q_z for two consecutive angles to allow matching of the data. This stitching process was demonstrated in this work and is shown in Figs. 8 and 9. For comparison, we include here the unstitched and unscaled data for the two samples measured in this work.

Figure 12 shows the unstitched and unscaled data for the silicon block. The data of the lower angle (black) and the higher angle (red) have an extensive overlap region to ensure appropriate stitching. For each angle, the data of the higher Q_z values measured are based on the neutrons with shorter wavelengths. It is notable that the data become quite noisy at the high Q_z end for each angle, and these data have been excluded from the stitched data shown in Fig. 8. These noisy data are visible in the first sub-frame (short wavelengths) in the ToF spectrum shown in Fig. 5 where the reflection signal is comparable to the background for these wavelengths. The other notable feature in the unscaled data is that the plateau of the total reflection is lower than one. For all the data measured (both samples), a simple scaling factor was required to correct this plateau to unity.

The unscaled and unstitched data of the monochromator sample are shown in Figs. 13 and 14. Both show well matched data measured under two different angles. The Q_z resolution is different due to different slit settings. The final data shown in Fig. 9 are obtained by stitching the data measured under different angles. For both

FIG. 12. Data of the silicon block measured with the WFM mode at V20. Measurements were carried out under incident angles of 0.29° (black) and 0.59° (red), respectively. The Fresnel reflectivity of a silicon substrate is used as a reference.
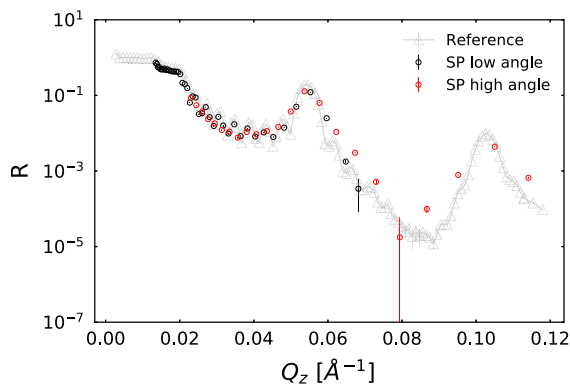
FIG. 13. Data of the monochromator sample measured with the SP mode at V20. Measurements were carried out under incident angles of 0.56° (black) and 0.96° (red), respectively. A reference curve measured with unpolarized neutrons at the V6 reflectometer is shown in gray for comparison.
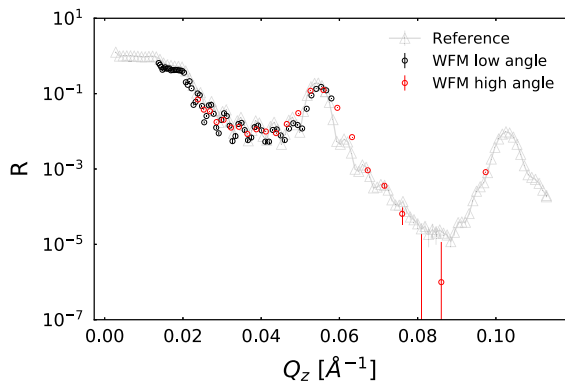
FIG. 14. Data of the monochromator sample measured with the WFM mode at V20. Measurements were carried out under incident angles of 0.56° (black) and 0.96° (red), respectively. A reference curve measured with unpolarized neutrons at the V6 reflectometer is shown in gray for comparison.

WFM and SP modes, using the same correction factor in R obtained for the measurements of the silicon block as described above leads to congruent datasets of the measurements and the reference data. Data measured with the WFM mode result in a smaller Q_z-range with respect to the data measured with the SP mode because the wavelength band is about 1 Å shorter.

DATA AVAILABILITY

Raw data were generated at the research reactor BER II large scale facility. Derived data supporting the findings of this study are available from the corresponding author upon reasonable request.

REFERENCES

[1]See http://www.reflectometry.net/reflect.htm for information about neutron reflectometers worldwide; accessed 18 February 2020.

[2]J. Schmitt, T. Gruenewald, G. Decher, P. S. Pershan, K. Kjaer, and M. Loesche, Macromolecules **26**, 7058 (1993).

[3]A. Ronneburg, M. Trapp, R. Cubitt, L. Silvi, S. Cap, M. Ballauff, and S. Risse, Energy Storage Mater. **18**, 182 (2019).

[4]G. P. Felcher, J. Appl. Phys. **87**, 5431 (2000).

[5]R. Garoby, A. Vergara, H. Danared, I. Alonso, E. Bargallo, B. Cheymol, C. Darve, M. Eshraqi, H. Hassanzadegan, A. Jansson, I. Kittelmann, Y. Levinsen, M. Lindroos, C. Martins, Ø. Midttun, R. Miyamoto, S. Molloy, D. Phan, A. Ponton, E. Sargsyan, T. Shea, A. Sunesson, L. Tchelidze, C. Thomas, M. Jensen, W. Hees, P. Arnold, M. Juni-Ferreira, F. Jensen, A. Lundmark, D. McGinnis, N. Gazis, J. Weisend II, M. Anthony, E. Pitcher, L. Coney, M. Gohran, J. Haines, R. Linander, D. Lyngh, U. Oden, H. Carling, R. Andersson, S. Birch, J. Cereijo, T. Friedrich, T. Korhonen, E. Laface, M. Mansouri-Sharifabad, A. Monera-Martinez, A. Nordt, D. Paulic, D. Piso, S. Regnell, M. Zaera-Sanz, M. Aberg, K. Breimer, K. Batkov, Y. Lee, L. Zanini, M. Kickulies, Y. Bessler, J. Ringnér, J. Jurns, A. Sadeghzadeh, P. Nilsson, M. Olsson, J.-E. Presteng, H. Carlsson, A. Polato, J. Harborn, K. Sjögreen, G. Muhrer, and F. Sordo, Phys. Scr. **93**, 014001 (2017).

[6]K. H. Andersen, D. N. Argyriou, A. J. Jackson, J. Houston, P. F. Henry, P. P. Deen, R. ToFt-Petersen, P. Beran, M. Strobl, T. Arnold, H. Wacklin-Knecht, N. Tsapatsaris, E. Oksanen, R. Woracek, W. Schweika, D. Mannix, A. Hiess, S. Kennedy, O. Kirstein, S. Petersson Årsköld, J. Taylor, M. E. Hagen, G. Laszlo, K. Kanaki, F. Piscitelli, A. Khaplanov, I. Stefanescu, T. Kittelmann, D. Pfeiffer, R. Hall-Wilton, C. I. Lopez, G. Aprigliano, L. Whitelegg, F. Y. Moreira, M. Olsson, H. N. Bordallo, D. Martín-Rodríguez, H. Schneider, M. Sharp, M. Hartl, G. Nagy, S. Ansell, S. Pullen, A. Vickery, A. Fedrigo, F. Mezei, M. Arai, R. K. Heenan, W. Halcrow, D. Turner, D. Raspino, A. Orszulik, J. Cooper, N. Webb, P. Galsworthy, J. Nightingale, S. Langridge, J. Elmer, H. Frielinghaus, R. Hanslik, A. Gussen, S. Jaksch, R. Engels, T. Kozielewski, S. Butterweck, M. Feygenson, P. Harbott, A. Poqué, A. Schwaab, K. Lieutenant, N. Violini, J. Voigt, T. Brückel, M. Koenen, H. Kämmerling, E. Babcock, Z. Salhi, A. Wischnewski, A. Heynen, S. Désert, J. Jestin, F. Porcher, X. Fabrèges, G. Fabrèges, B. Annighöfer, S. Klimko, T. Dupont, T. Robillard, A. Goukassov, S. Longeville, C. Alba-Simionesco, P. Bourges, J. Guyon Le Bouffy, P. Lavie, S. Rodrigues, E. Calzada, M. Lerche, B. Schillinger, P. Schmakat, M. Schulz, M. Seifert, W. Lohstroh, W. Petry, J. Neuhaus, L. Loaiza, A. Tartaglione, A. Glavic, S. Schütz, J. Stahn, E. Lehmann, M. Morgano, J. Schefer, U. Filges, C. Klauser, C. Niedermayer, J. Fenske, G. Nowak, M. Rouijaa, D. J. Siemers, R. Kiehn, M. Müller, H. Carlsen, L. Udby, K. Lefmann, J. O. Birk, S. Holm-Dahlin, M. Bertelsen, U. B. Hansen, M. A. Olsen, M. Christensen, K. Iversen, N. B. Christensen, H. M. Rønnow, P. G. Freeman, B. C. Hauback, R. Kolevatov, I. Llamas-Jansa, A. Orecchini, F. Sacchetti, C. Petrillo, A. Paciaroni, P. Tozzi, M. Zanatta, P. Luna, I. Herranz, O. G. del Moral, M. Huerta, M. Magán, M. Mosconi, E. Abad, J. Aguilar, S. Stepanyan, G. Bakedano, R. Vivanco, I. Bustinduy, F. Sordo, J. L. Martínez, R. E. Lechner, F. J. Villacorta, J. Šaroun, P. Lukáš, M. Markó, M. Zanetti, S. Bellissima, L. del Rosso, F. Masi, C. Bovo, M. Chowdhury, A. De Bonis, L. Di Fresco, C. Scatigno, S. F. Parker, F. Fernandez-Alonso, D. Colognesi, R. Senesi, C. Andreani, G. Gorini, G. Scionti, and A. Schreyer, Nucl. Instrum. Methods Phys. Res., Sect. A **957**, 163402 (2020).

[7]F. Mezei, The ESS Project 2, 2002.

[8]K. Lieutenant and F. Mezei, J. Neutron Res. **14**, 177 (2006).

[9]F. Mezei and M. Russina, "Advances in neutron scattering instrumentation," Proc. SPIE **4785**, 24–33 (2002).

[10]H. Wacklin and A. Vickery, FREIA Instrument Proposal (ESS-0183681), 2014.

[11]D. Nekrassov, C. Zendler, and K. Lieutenant, Nucl. Instrum. Methods Phys. Res., Sect. A **716**, 71 (2013).

[12]F. Mezei, J. Phys. Soc. Jpn. **82**, SA025 (2013).

[13]M. Strobl, Phys. Procedia **69**, 18 (2015).

[14]P. Schmakat, M. Seifert, M. Schulz, A. Tartaglione, M. Lerche, M. Morgano, P. Böni, and M. Strobl, Nucl. Instrum. Methods Phys. Res., Sect. A **979**, 164467 (2020).

[15]W. Schweika, N. Violini, K. Lieutenant, C. Zendler, D. Nekrassov, A. Houben, P. Jacobs, and P. F. Henry, J. Phys.: Conf. Ser **746**, 012013 (2016).

[16]A. Fedrigo, D. Colognesi, M. Bertelsen, M. Hartl, K. Lefmann, P. P. Deen, M. Strobl, F. Grazzi, and M. Zoppi, Rev. Sci. Instrum. **87**, 065101 (2016).

[17]A. J. Jackson, K. Kanaki, C. I. Lopez, C. Zenlder, E. Nilsson, G. Nagy, N. Cherkashyna, A. Sandstrom, T. Nielsen, A. Pettersson, S. A. Pullen, P. M. Bentley, T. Gahl, R. Hall-Wilton, I. Sutton, and K. H. Andersen,

JAEA-CONF–2015-002, **48**, 263 (2016), see https://inis.iaea.org/search/search.aspx?orig_q=RN:48014673.

[18] M. Strobl, M. Bulat, and K. Habicht, Nucl. Instrum. Methods Phys. Res., Sect. A **705**, 74 (2013).

[19] R. Woracek, T. Hofmann, M. Bulat, M. Sales, K. Habicht, K. Andersen, and M. Strobl, Nucl. Instrum. Methods Phys. Res., Sect. A **839**, 102 (2016).

[20] I. Stefanescu, M. Christensen, J. Fenske, R. Hall-Wilton, P. F. Henry, O. Kirstein, M. Müller, G. Nowak, D. Pooley, D. Raspino, N. Rhodes, J. Šaroun, J. Schefer, E. Schooneveld, J. Sykora, and W. Schweika, J. Instrum. **12**, P01019 (2017).

[21] R. Woracek, M. Krzyzagorski, H. Markötter, P. M. Kadletz, N. Kardjilov, I. Manke, and A. Hilger, Opt. Express **27**, 26218 (2019).

[22] D. Pooley, J. Lee, F. Akeroyd, O. Arnold, M. Hart, J. John, P. Kadletz, W. Kockelmann, T. Minniti, C. Moreton-Smith, M. Morgano, N. Rhodes, E. Schooneveld, I. Sedgwick, C. Vallance, and R. Woracek, *Neutron Radiography: WCNR-11* (Materials Research Forum LLC, 2020).

[23] A. Backis, A. Khaplanov, R. A. Jebali, R. Ammer, I. Apostolidis, J. Birch, C. C. Lai, P. P. Deen, M. Etxegarai, N. de Ruette, J. F. Ramos, D. F. Förster, E. Haettner, R. Hall-Wilton, D. Hamilton, C. Höglund, P. M. Kadletz, K. Kanaki, E. Karnickis, O. Kirstein, S. Kolya, Z. Kraujalyte, A. Laloni, K. Livingston, O. Löhman, V. Maulerova, N. Mauritzon, F. Müller, I. L. Higuera, T. Richter, L. Robinson, R. Roth, M. Shetty, J. Taylor, R. Woracek, and W. Xiong, "Time- and energy-resolved effects in the boron-10 based Multi-Grid and helium-3 based thermal neutron detector," Meas. Sci. Technol. (published online, 2020).

[24] V. Maulerova, K. Kanaki, P. M. Kadletz, R. Woracek, T. Wilpert, K. Fissum, A. Laloni, N. Mauritzson, F. Issa, and R. Hall-Wilton, Phys. Rev. Accel. Beams **23**, 072901 (2020).

[25] P. Jorba, M. Schulz, D. S. Hussey, M. Abir, M. Seifert, V. Tsurkan, A. Loidl, C. Pfleiderer, and B. Khaykovich, J. Magn. Magn. Mater. **475**, 176 (2019).

[26] D. F. Förster, F. Müller, U. Giesen, B. Lindenau, T. Ortmanns, J. Wolters, U. Pabst, M. Butzek, R. Woracek, T. Kozielewski, and M. Monkenbusch, Nucl. Instrum. Methods Phys. Res., Sect. A **908**, 298 (2018).

[27] V. Maulerova, J. Nilsson, M. Olsson, S. Alcock, A. Quintanilla, D. Zielinski, A. Mukai, F. Issa, S. Kolya, W. Smith, D. Broderick, K. Löki, J. Sparger, R. Woracek, J. Taylor, T. Richter, R. Hall-Wilton, O. Kirstein, and N. Tsapatsaris, EPL **128**, 52001 (2019).

[28] E. Babcock, Z. Salhi, R. Gainov, R. Woracek, H. Soltner, P. Pistel, F. Beule, K. Bussmann, A. Heynen, H. Kämmerling, F. Suxdorf, M. Strobl, M. Russina, J. Voigt, and A. Ioffe, J. Phys.: Conf. Ser. **862**, 012002 (2017).

[29] E. Babcock, Z. Salhi, R. Gainov, R. Woracek, H. Soltner, P. Pistel, F. Beule, K. Bussmann, A. Heynen, H. Kämmerling, F. Suxdorf, M. Strobl, M. Russina, J. Voigt, and A. Ioffe, "Towards wide-angle neutron polarization analysis with a ^{3}He spin filter for TOPAS and NEAT: Testing magic pastis on V20 at HZB," AIP Conf. Proc. **1969**, 050005 (2018).

[30] M. Strobl, R. Harti, C. Gruenzweig, R. Woracek, and J. Plomp, J. Imaging **3**, 64 (2017).

[31] T. Maimaitiyili, R. Woracek, M. Neikter, M. Boin, R. Wimpory, R. Pederson, M. Strobl, M. Drakopoulos, N. Schäfer, and C. Bjerkén, Materials **12**, 667 (2019).

[32] M. Siegwart, R. Woracek, J. I. Márquez Damián, A. S. Tremsin, V. Manzi-Orezzoli, M. Strobl, T. J. Schmidt, and P. Boillat, Rev. Sci. Instrum. **90**, 103705 (2019).

[33] A. A. van Well, Physica B **180-181**, 959 (1992).

[34] M. Russina, F. Mezei, and G. Kali, J. Phys.: Conf. Ser. **340**, 012018 (2012).

[35] M. Russina, G. Káli, Z. Sánta, and F. Mezei, Nucl. Instrum. Methods Phys. Res., Sect. A **654**, 383 (2011).

[36] User manual and technical specification denex-300tn.

[37] A. H. C. Mukai, M. J. Clarke, M. J. Christensen, J. M. C. Nilsson, M. G. Shetty, M. Brambilla, D. Werder, M. Könnecke, J. Harper, M. D. Jones, F. A. Akeroyd, C. Reis, G. Kourousias, and T. S. Richter, J. Instrum. **13**, T10001 (2018).

[38] M. D. Jones, F. A. Akeroyd, O. Arnold, M. J. Clarke, N. Draper, M. Gigg, L. Moore, and T. Richter, J. Phys.: Conf. Ser. **1021**, 012013 (2018).

[39] See https://nicos-controls.org/ for information about the open-source scientific instrument control software NICOS.

[40] See https://epics.anl.gov/ for information about the open-source Experimental Physics and Industrial Control System EPICS.

[41] See https://kafka.apache.org/ for information about the open-source event streaming platform Apache Kafka.

[42] See http://www.phillipsscientific.com/pdf/715ds.pdf for technical information about the utilized constant fraction timing discriminator.

[43] See https://www.ortec-online.com/-/media/ametekortec/manuals/566-mnl.pdf for technical information about the utilized Time-to-Amplitude Converter.

[44] See indico.esss.lu.se/event/858/contributions/6716/attachments/6515/9376/2_adc_demonstrator.pdf for Ikon presentation.

[45] M. J. Christensen, M. Shetty, J. Nilsson, A. Mukai, R. A. Jebali, A. Khaplanov, M. Lupberger, F. Messi, D. Pfeiffer, F. Piscitelli, T. Blum, C. Søgaard, S. Skelboe, R. Hall-Wilton, and T. Richter, J. Instrum. **13**, T11002 (2018).

[46] See http://www.hdfgroup.org/hdf5/ for information about the Hierarchical Data Format (HDF).

[47] M. Könnecke, F. A. Akeroyd, H. J. Bernstein, A. S. Brewster, S. I. Campbell, B. Clausen, S. Cottrell, J. U. Hoffmann, P. R. Jemian, D. Männicke, R. Osborn, P. F. Peterson, T. Richter, J. Suzuki, B. Watts, E. Wintersberger, and J. Wuttke, J. Appl. Crystallogr. **48**, 301 (2015).

[48] O. Arnold, J. C. Bilheux, J. M. Borreguero, A. Buts, S. I. Campbell, L. Chapon, M. Doucet, N. Draper, R. Ferraz Leal, M. A. Gigg, V. E. Lynch, A. Markvardsen, D. J. Mikkelson, R. L. Mikkelson, R. Miller, K. Palmen, P. Parker, G. Passos, T. G. Perring, P. F. Peterson, S. Ren, M. A. Reuter, A. T. Savici, J. W. Taylor, R. J. Taylor, R. Tolchenov, W. Zhou, and J. Zikovsky, Nucl. Instrum. Methods Phys. Res., Sect. A **764**, 156 (2014).

[49] S. Heybrock, O. Arnold, I. Gudich, D. Nixon, and N. Vaytet, J. Neutron Res. **22**, 169–181 (2020).

[50] See https://docs.scipy.org/doc/scipy/reference/generated/scipy.signal.find_peaks.html for information about the employed peak finding algorithm.

[51] A. A. van Well and H. Fredrikze, Physica B **357**, 204 (2005) [*Proceedings of the 8th International Conference on Surface X-ray and Neutron Scattering*].

[52] M. Trapp, "V6: The reflectometer at BER II," J. Large-Scale Res. Facil. JLSRF **3**, 114 (2017).